1 **Shortwave Radiative Impacts of the Asian Tropopause Aerosol Layer (ATAL)**

2 **using Balloon-borne In-situ measurements at three distinct locations in India**

3 Vadassery Neelamana Santhosh[1], Bomidi Lakshmi Madhavan[1], Sivan Thankamani Akhil

4 Raj[2], Madineni Venkat Ratnam[1], Jean-Paul Vernier[3,4], and Frank Gunther Wienhold[5]

5   [1]National Atmospheric Research Laboratory (NARL), Gadanki 517 112, India

6   [2]India Meteorological Department (IMD), New Delhi 110 003, India

7   [3]National Institute of Aerospace, Hampton, VA, USA

8   [4]NASA Langley Research Center, USA

9   [5]Institute of Atmospheric and Climate Science (IAC), ETH, Zurich, Switzerland

11 **Correspondence to**:
12   Bomidi Lakshmi Madhavan (madhavanbomidi@gmail.com, blmadhavan@narl.gov.in)

14 **Abstract**

15   This study aims to investigate the direct shortwave radiative forcing and heating rates of the

16 Asian Tropopause Aerosol Layer (ATAL) in the Upper Troposphere Lower Stratosphere (UTLS)

17 region using in-situ observations from the Balloon measurement campaigns of the Asian

18 Tropopause Aerosol Layer (BATAL) conducted between 2014 and 2018. Measurements were

19 obtained over three distinct locations in India: Gadanki (13.48°N, 79.18°E), Hyderabad (17.47°N,

20 78.58°E), and Varanasi (25.27°N, 82.99°E). Given the ambiguity in the chemical composition of

21 ATAL from several reported studies, seven different aerosol mixtures—comprising sulfate,

22 nitrate, organic carbon, and ammonium—were considered to assess their impact on estimates of

23 ATAL radiative forcing and heating rates. A pronounced enhancement in aerosol backscatter was

24 observed at ATAL altitudes (13 to 19 km) across all locations, with the backscatter ratio (at 455

25 nm) peaking at 1.07 over Varanasi and Hyderabad, followed by 1.06 over Gadanki. Radiative

forcing estimates indicate a net warming effect, with ATAL contributing up to 3% of the total columnar atmospheric forcing. Heating rates reveal a marked increase in aerosol-induced warming at ATAL altitudes, with maximum heating rates reaching 0.03 K day^{-1} across the study locations. The radiative impact of ATAL aerosols is highly sensitive to variations in the aerosol composition. Compared to a reference case with a stratospheric sulfate background, the ATAL radiative forcing varies between 0.03 and 0.28 W m^{-2} (1.5 to 14-fold increase). At the same time, heating rates exhibit a 30-fold increase, reaching 0.03 K day^{-1}, depending on the aerosol mixture. Despite these strong localized effects within the UTLS, the overall contribution to total columnar aerosol forcing remains moderate (up to 5%), underscoring the importance of aerosol composition in determining ATAL's radiative influence.

Keywords: *Asian Tropopause Aerosol Layer; Aerosol-Radiation Interaction; Radiative forcing and heating rates; Upper Troposphere-Lower Stratosphere*

1. Introduction

The Asian summer monsoon, which occurs from June to August, plays a crucial role in transporting pollutant-laden air masses across a vast geographic region in the Northern Hemisphere (e.g., Vogel et al., 2024; Yu et al., 2017). A large-scale anti-cyclonic circulation, known as the Asian Summer Monsoon Anticyclone (ASMA), develops in the Upper Troposphere Lower Stratosphere (UTLS) due to intense heating over the Tibetan Plateau, coupled with deep convection over the head Bay of Bengal (BoB). This system effectively traps and redistributes air masses within a broad region (10°N–40°N, 10°E–140°E) (von Hobe et al., 2021; Lelieveld et al., 2018; Park et al., 2007; Randel and Park, 2006), leading to significant enhancements in trace constituents such as water vapor, methane, nitrogen dioxide, ozone around the ASMA center (Basha et al., 2021; Kumar and Ratnam, 2021; Park et al., 2007). Satellite observations have

identified a persistent aerosol enhancement in the UTLS (~ 13–18 km) during the monsoon, known as the Asian Tropopause Aerosol Layer (ATAL) (Vernier et al., 2011, 2015; Thomason and Vernier, 2013). The ATAL is of particular scientific interest due to its potential influence on stratospheric composition, chemistry, cirrus cloud properties, and the Earth's radiative balance.

The formation and dissipation of ATAL are closely linked to deep convection, which transports aerosols from the BoB and surrounding land areas into the UTLS (He et al., 2020). However, ATAL aerosols exhibit significant spatial and temporal variability, reflecting their diverse sources and transport pathways (Fairlie et al., 2020; Lau et al., 2018; Neely et al., 2014; Fadnavis et al., 2013). The presence of both natural and anthropogenic aerosols within ATAL, combined with dynamic and chemical interactions—including secondary aerosol formation—further complicates its characterization. Recent studies indicate that a substantial fraction of ATAL aerosols results from gas-to-particle conversion of inorganic and organic precursors, highlighting the role of secondary aerosol formation in this region (Appel et al., 2022).

Despite growing interest in ATAL, its optical and radiative properties remain poorly constrained due to limitations in observational datasets. Aerosol optical depth (AOD) and extinction coefficient measurements in the UTLS are hindered by low aerosol concentrations, instrumental detection thresholds, and retrieval uncertainties in satellite and lidar observations. Additionally, complex transport and mixing processes in the UTLS make it challenging to determine ATAL's chemical composition, which is critical for quantifying its optical properties— such as single scattering albedo (SSA) and asymmetry parameter (ASY)—that govern radiative transfer calculations. Early studies primarily identified sulfate as the dominant component of ATAL (e.g., Vernier et al., 2015; Yu et al., 2015; Fadnavis et al., 2013). However, subsequent investigations revealed a more diverse aerosol composition. A reanalysis study for the summer of

72 2008 detected significant contributions from mineral dust and carbonaceous aerosols transported

73 by deep convection (Lau et al., 2018). Long-term simulations (2000–2015) using the Community

74 Earth System Model further indicated that ATAL aerosols comprise approximately 40% sulfate,

75 30% secondary aerosols, 15% primary aerosols, 14% ammonia-based aerosols, and trace amounts

76 of black carbon (Bossolasco et al., 2021). Additionally, combined satellite, high-altitude aircraft,

77 and cloud-chamber studies suggested the dominance of ammonium nitrate particles in the upper

78 troposphere (Höpfner et al., 2019). Several in situ studies have also reported a substantial nitrate

79 fraction in ATAL (e.g., Vernier et al., 2022; Vernier et al., 2018), with aircraft-based chemical

80 analyses indicating significant contributions from particulate nitrate, ammonium, and organic

81 aerosols at 13–18 km (Appel et al., 2022).

82   Understanding the radiative impacts of ATAL remains a major research challenge due to the

83 uncertainties in aerosol composition, optical properties, and vertical distribution. Limited studies

84 have quantified its radiative effects. Vernier et al. (2015) reported an increase in summertime AOD

85 over Asia associated with ATAL from 0.002 to 0.006 between 1995 and 2013, leading to a regional

86 shortwave radiative forcing of -0.12 W m^{-2} at the top of the atmosphere (TOA). This forcing

87 partially offset (~33%) the radiative impact of global CO_2 increases during 2000–2010 (Solomon

88 et al., 2011). Using MERRA-2 reanalysis, Gao et al. (2023) estimated that ATAL aerosols exert a

89 clear-sky positive radiative forcing of 0.15 W m^{-2} at 20 km due to their absorption properties.

90 Chemistry-climate modeling by Fadnavis et al. (2022) further demonstrated that carbonaceous

91 aerosols induce tropospheric and lower stratospheric heating of 0.02–0.3 K per month, thereby

92 enhancing water vapor transport into the UTLS. Similarly, Chavan et al. (2021) showed that

93 biomass-burning aerosols over Asia contribute to UTLS heating rates of 0.001–0.02 K day^{-1}.

Despite these insights, significant gaps remain in our understanding of ATAL's radiative effects. The contribution of ATAL aerosols to total atmospheric forcing is largely unknown, and real-time, high-resolution, altitudinal in-situ observations remain scarce. Moreover, previous estimates rely predominantly on reanalysis or model-based studies, which introduce uncertainties due to several assumptions. Therefore, there is a need for direct observational constraints on ATAL radiative forcing and heating rates.

To address these gaps, the Balloon measurement campaigns for the Asian Tropopause Aerosol Layer (BATAL) provide high-resolution in-situ measurements of aerosol and atmospheric properties, offering a unique opportunity to refine radiative transfer calculations for ATAL. This study leverages BATAL observations to (i) characterize ATAL enhancements across multiple BATAL study locations, (ii) quantify ATAL radiative forcing and heating rates within the UTLS (12-20 km) using the high-resolution in-situ measurements, (iii) assess the contribution of ATAL to total atmospheric column forcing, (iv) ascertain the sensitivity of ATAL radiative forcing and heating rates to variations in aerosol compositions, and (v) compare the heating rate estimates from in-situ measurements from the three-point locations with spatially averaged estimated derived from satellite observations to ascertain their regional representativeness and variability. To achieve these objectives, we introduce a methodological framework that integrates in-situ data to screen clouds, identify potential aerosol types or compositions, and incorporate these observations into radiative transfer calculations.

The paper is structured as follows: Section 2 provides a brief description of the BATAL and study locations, Section 3 details the datasets used, and Section 4 outlines the methodology for estimating radiative impacts. The results are discussed in Section 5, followed by a summary of key findings in Section 6.

2. Campaign Details and Observation Sites

The BATAL campaigns were conducted jointly by the Indian Space Research Organization (ISRO) and the National Aeronautics and Space Administration (NASA) during the late monsoon season (July –September) from 2014 to 2018. These campaigns deployed high-altitude balloons equipped with miniature payloads to investigate the optical properties, size distribution, and composition of aerosols in the ATAL. Additionally, the campaigns focused on examining the behavior of ozone and water vapor in the UTLS and assessing the role of deep convection in transporting aerosols and trace gases to this region. For detailed descriptions of the payloads, balloon specifications, and other scientific objectives, refer to Vernier et al. (2018).

The BATAL campaigns were conducted at three distinct sites in India, chosen based on their local weather, emission characteristics, and recovery of payload (**Fig. 1**):

(i) **Gadanki (13.48°N, 79.18°E)** – A rural background location in southern peninsular India with hilly topography. Aerosol sources in this region are primarily from vehicular emissions, agricultural activities, and wood burning. During the monsoon season, the site experiences surface pressures between 960 and 965 hPa, temperatures ranging from 27°C to 30°C, and prevailing southwesterly winds of 1.5 to 1.6 m s^{-1}. The relative humidity is typically below 60%. Sky radiometer observations from this location revealed the presence of dominant coarse-mode aerosols during the monsoon (Santhosh et al., 2024a; Madhavan et al., 2021).

(ii) **Hyderabad (17.47°N, 78.58°E)** – A rapidly urbanizing megacity situated on the Deccan Plateau. This region has a semi-arid climate characterized by significant seasonal variations in temperature and humidity. Anthropogenic sources primarily drive local emissions, whereas long-range aerosol transport is more prevalent during the monsoon

140   season. AOD measurements indicate that coarse-mode aerosols contribute significantly

141   to the overall aerosol burden (Ratnam et al., 2020; Sinha et al., 2013).

142   (iii) **Varanasi (25.27°N, 82.99°E)** – An urban site in the Indo-Gangetic Plain (IGP)

143   characterized by a humid subtropical climate with pronounced seasonal variations in

144   temperature and rainfall. The region experiences high aerosol loading due to a mix of

145   natural and anthropogenic sources. Coarse-mode aerosols, primarily dust, dominate in

146   the pre-monsoon months, while fine-mode anthropogenic aerosols, including

147   carbonaceous and sulfate aerosols, are more prominent during the post-monsoon and

148   winter months (Murari et al., 2017; Tiwari and Singh, 2013).

149
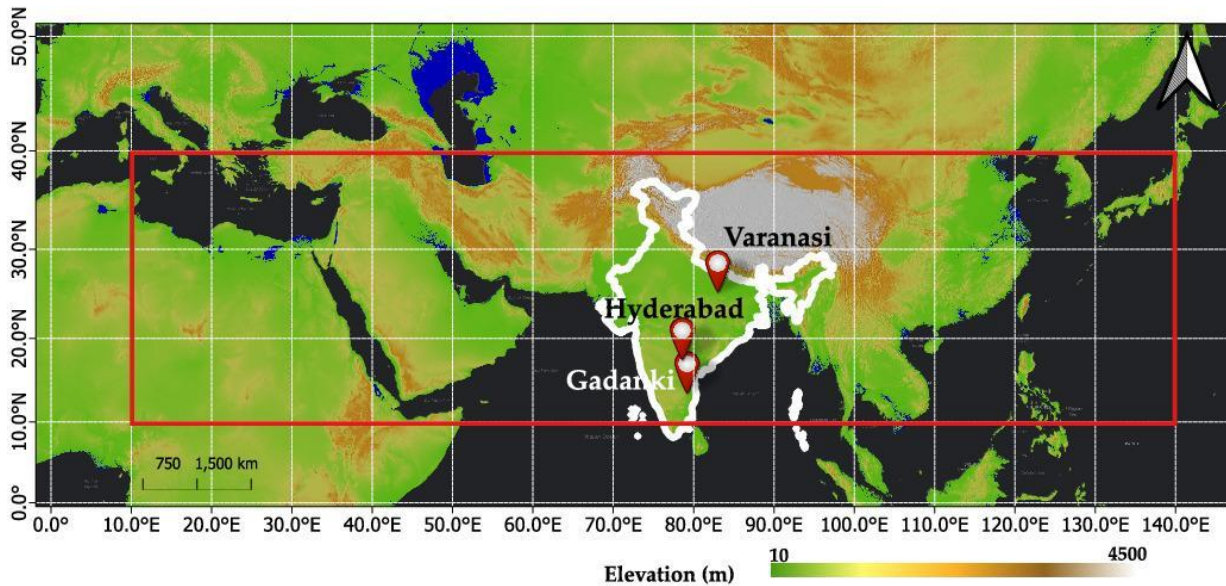
150 **Figure 1:** Balloon launch sites during the 2014-2018 BATAL campaigns. The red box outlines
151 the typical geographic extent of the Asian Tropopause Aerosol Layer (ATAL) region, spanning
152 10°E–140°E and 10°N–40°N.

153   These strategically selected sites offer critical insights into the spatial variability of aerosols

154 that influence the ATAL, enabling a comprehensive assessment of their chemical composition,

155 transport pathways, and radiative impacts in the UTLS.

3. Datasets

Among the multiple payloads launched during the BATAL campaigns, this study focuses on measurements from radiosondes and ozonesondes (for atmospheric parameters) and the Compact Optical Backscatter Aerosol Detector (COBALD) (for aerosol measurements).

3.1. Radiosonde and Ozonesonde

We utilized pressure, temperature, and relative humidity (RH) data from radiosondes, along with ozone volume mixing ratios from ozonesondes, to generate user-defined atmospheric profiles for the radiative forcing calculations. The Meisei (RS-11 G) and iMet radiosondes were used to measure temperature and pressure at different altitudes. The iMet radiosondes employed piezo-resistors for atmospheric pressure measurements, with an accuracy of 1–2 hPa. The Meisei radiosonde, which lacks a pressure sensor, derived pressure values from temperature and GPS altitude data. Ozone mixing ratios were obtained using EN-SCI Electrochemical Concentration Cell (ECC) ozonesondes, following the methodology outlined by Komhyr et al. (1995). More details on these methodologies can be found in Ratnam et al. (2014) and Akhil Raj et al. (2015). The observed atmospheric parameter profiles in the UTLS region are shown in **Figure S1**.

3.2. Compact Optical Backscatter Aerosol Detector (COBALD)

COBALD, developed by ETH Zurich, is a lightweight, balloon-borne sonde designed to measure backscattered light from aerosols, molecules, and clouds (Vernier et al., 2018). It operates with two LED light sources emitting at 455 nm (blue) and 940 nm (red) wavelengths. The emitted light illuminates the surrounding air, and a silicon photodetector captures the backscattered signal from particles within a 0.5-meter range. Approximately 90% of the measured backscattering signal originates from within a 10-meter radius of the instrument. COBALD operates without requiring external airflow and transmits real-time backscatter data, alongside pressure and temperature

179   measurements, to the ground station at a frequency of 1 Hz. The instrument has an uncertainty of

180   5% and a precision better than 1% in the UTLS region (Vernier et al., 2015, 2018).

181   Details of the balloon launches from which the present study's measurements were obtained

182   are summarized in **Table 1**. We considered those balloon-borne in-situ measurements, which

183   covered a minimum altitude of 20 km above the surface, to capture the ATAL signal effectively.

184   **Table 1:** Summary of balloon launches during the BATAL campaigns, highlighting the
185   availability of Compact Optical Backscatter Aerosol Detector (COBALD), radiosonde, and
186   ozonesonde measurements. All measurements cover a minimum altitude of 20 km, with maximum
187   altitudes ranging from 25 to 35 km. The average maximum altitude is 29 km at Gadanki, 27 km at
188   Hyderabad, and 30 km at Varanasi. 'Y' indicates data availability for a specific payload, while 'N'
189   denotes non-availability. All launches were conducted during local nighttime (UTC +05:30).

Location	Date and Time (UTC) of launch	COBALD	Ozonesonde	Radiosonde
Gadanki **(13.48°N, 79.18°E)**	18-08-2014, 15:00	Y	N	Y
	19-08-2014, 15:30	Y	Y	Y
	07-09-2016, 19:50	Y	Y	Y
	09-09-2016, 15:00	Y	Y	Y
	31-07-2017, 18:00	Y	Y	Y
	01-08-2017, 18:00	Y	Y	Y
Hyderabad **(17.47°N, 78.58°E)**	01-08-2015, 17:00	Y	N	Y
	05-08-2015, 22:00	Y	Y	Y
	06-08-2015, 22:00	Y	Y	Y
	08-08-2015, 18:00	Y	N	Y
	09-08-2015, 22:00	Y	N	Y
	13-08-2015, 18:00	Y	Y	Y
	08-08-2018, 21:00	Y	Y	Y
	17-08-2018, 20:00	Y	Y	Y

	26-08-2018, 20:00	Y	Y	Y
	28-08-2018, 20:20	Y	Y	Y
Varanasi	22-08-2015, 18:00	Y	N	Y
(25.27°N, 82.99°E)	22-08-2015, 22:00	Y	N	Y
	04-08-2016, 23:00	Y	N	Y
	06-08-2016, 21:00	Y	Y	Y
	08-08-2016, 21:30	Y	Y	Y

190

3.3. Ancillary Datasets

192 In addition to in-situ measurements, we utilized the following ancillary datasets:

193 **(i) MERRA-2 Reanalysis:** We used the Modern-Era Retrospective analysis for Research and

194 Applications, Version 2 (MERRA-2), Hourly, Time-averaged, Single-Level, Assimilation,

195 Aerosol Diagnostics dataset (M2T1NXAER; $0.625° \times 0.5°$ resolution, V5.12.4) developed

196 by NASA's Global Modelling and Assimilation Office (GMAO) to retrieve AOD values

197 for the campaign period. These AOD values were used to normalize aerosol extinction

198 profiles, ensuring consistency between columnar aerosol loading and derived extinction

199 profiles (for example, Santhosh et al., 2024b). Since collocated nighttime AOD retrievals

200 from in-situ measurements were unavailable, MERRA-2 served as a reliable alternative.

201 Che et al. (2019) reported improved MERRA-2 AOD performance in the South Asian

202 region based on comparisons with AERONET observations. The dataset provides total

203 AOD at 550 nm and the Angstrom exponent (AE) for the 470-870 nm range. The AODs at

204 455 and 940 nm wavelengths were derived using the Angstrom power law (Angstrom,

205 1964):

206
$$AOD_{\lambda_0} = AOD_{550} \times \left(\frac{\lambda_0}{550}\right)^{-AE} \qquad (1)$$

207   where λ_0 represents the target wavelength. Given that our required wavelengths (455 nm

208   and 940 nm) fall slightly outside the 470-870 nm range, we assumed the power-law

209   relationship remains valid. Across study locations, Varanasi had the highest mean

210   nighttime AOD at 550 nm (0.37 ± 0.13) from 19:30 to 05:30 local time, followed by

211   Hyderabad (0.28 ± 0.05) and Gadanki (0.26 ± 0.07).

212   **(ii) Moderate Resolution Imaging Spectroradiometer (MODIS):** Surface reflectance is a

213   critical parameter in aerosol radiative forcing calculations. We used the MCD43A4 Nadir

214   Bidirectional Reflectance Distribution Function (BRDF)-Adjusted Reflectance (NBAR)

215   product. This dataset (MODIS/Terra Nadir BRDF-Adjusted Reflectance Daily L3 Global

216   500m SIN Grid) provides spectral reflectance values at MODIS spectral band (centered at

217   0.469, 0.555, 0.645, 0.859, 1.24, 1.64, and 2.13 μm) at local solar noon

218   (https://lpdaac.usgs.gov/product/mcd43a4v061). Surface reflectance values were found to

219   be similar across study locations in the visible spectrum, with deviations in the infrared

220   range. Among the sites, Hyderabad exhibited the highest reflectance, while Varanasi had

221   the lowest (**Fig. S2**).

222   **4. Methods**

223   The methodology followed in this study (**Fig. 2**) is discussed in the following subsections.

224   **4.1. Cloud Screening of the COBALD Profiles**

225   COBALD measurements capture total backscattered light from a mixture of aerosols, clouds,

226   and molecules. Isolating aerosol contributions from the total backscatter becomes challenging in

227   the presence of clouds, necessitating the identification and exclusion of these cloud-contaminated

228   in-situ measurements. The total backscatter signal is typically expressed as the backscatter ratio

229   (BSR), defined as:

230
$$BSR = \frac{\beta_{Total}}{\beta_{mol}} \qquad (2)$$

231   where β_{mol} represents the molecular backscatter coefficient, while β_{Total} includes both particle and

232   molecular contributions. In cloud-free conditions, $\beta_{Total} = \beta_{mol} + \beta_{aer}$, where β_{aer} is the aerosol

233   backscatter coefficient.

234
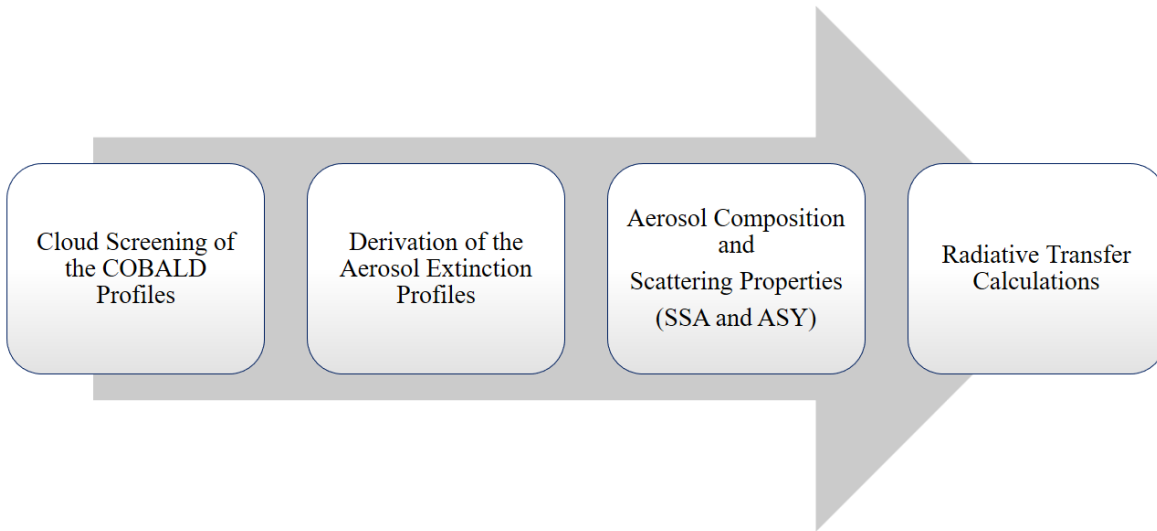
235   **Figure 2:** Schematic representation of the methodology used in this study. SSA and ASY refer to
236   single scattering albedo and asymmetry parameter, respectively.

237   The color index (CI) is defined as the 940-to-455nm ratio of the aerosol component of BSR:

238
$$CI = \frac{BSR_{940} - 1}{BSR_{455} - 1} \qquad (3)$$

239   CI is independent of particle number concentration and serves as a useful metric for

240   interpreting particle size. Both BSR and CI are indicators of aerosol presence. Cirrus clouds can

241   be identified separately using BSR at 455 nm and 940 nm or through CI, which enables

242   discrimination between ice particles (CI < 7) and aerosol (CI > 7) (Hanumanthu et al., 2020). Based

243 on previous studies, we set the following cloud screening criteria (above 10 km):

- BSR$_{455}$ < 1.12 for the blue channel measurements, similar to Akhil Raj et al. (2022).

245 - BSR940 < 2.5 and CI > 7 for the red channel following Vernier et al. (2015).

246 Since these cloud screening criteria have not been validated in the lower atmosphere, we

247 employed an alternative approach that combines vertical gradients of air temperature and relative

248 humidity (RH) with altitude-dependent RH thresholds, as described in Xu et al. (2023), in the

249 lower atmosphere (below 10 km). While radiosonde data provide measurements in the UTLS and

250 beyond, this method may introduce uncertainties at higher altitudes due to radiosonde limitations

251 associated with the accuracy of RH measurements (Miloshevich et al., 2006). A detailed

252 description of this method is provided in the Supplement (**Section S1**), along with relevant relative

253 humidity (RH) thresholds (**Table S1**) and an example (**Fig. S3**).

254 Based on the above methodology, a backscatter ratio profile influenced by molecules and

255 aerosols is derived from the surface to the maximum altitude of a given COBALD measurement.

256 **4.2. Derivation of the Aerosol Extinction Profiles**

257 Under cloud-free conditions, the aerosol backscatter coefficient β_{aer} (expressed in m^{-1} sr^{-1}) at a

258 given wavelength λ and altitude z is obtained from **Eq. (2)**:

$$\beta_{aer,\lambda}(z) = \beta_{mol,\lambda}(z) \times (BSR(z) - 1) \qquad (4)$$

260 The molecular backscatter coefficients β_{mol} (expressed in m^{-1} sr^{-1}) are determined using the in-

261 situ temperature and pressure profiles from radiosonde measurements (Collis and Russell, 2005)

262 using the following equation:

$$\beta_{mol,\lambda}(z) = \frac{P(z)}{R_d T(z) M} \left(\frac{\lambda}{550}\right)^{-4.09} \times 10^{-32} \qquad (5)$$

264   where $R_d = 287$ J K^{-1} kg^{-1} is the gas constant for dry air, and M $= 4.81 \times 10^{32}$ kg is the molecular

265   weight of dry air. The aerosol backscatter coefficients were multiplied by a lidar ratio of 40 sr to

266   derive extinction coefficient profiles, consistent with previous studies over the Indian region (e.g.,

267   Gupta et al., 2021).

268   To reduce uncertainties in lidar ratios, the aerosol extinction coefficient profiles $\beta_{ext}(z)$ at

269   wavelength λ were normalized using MERRA-2 AOD:

270    $$\beta_{ext,scaled}(\lambda, z) = \beta_{ext}(\lambda, z) \times \frac{AOD_{MERRA-2}(\lambda)}{AOD_{COBALD}(\lambda)} \qquad (6)$$

271   where AOD$_{COBALD}(\lambda)$ represents the AOD obtained by integrating the derived aerosol

272   extinction profile (with a lidar ratio of 40 sr). This normalization ensures consistency between the

273   columnar loading and extinction profiles, reducing biases in the estimates of aerosol direct

274   radiative effects (Santhosh et al., 2024b).

275   **4.3. Aerosol Composition and Scattering Properties**

276   The composition of aerosols in the UTLS region during ATAL periods remains highly variable

277   across different measurement techniques and time periods, posing a significant challenge for

278   accurate characterization (**Table 2**). Despite differences, multiple studies consistently report the

279   presence of sulfates, nitrates, organic carbon, and ammonium aerosols in varying proportions.

280   **Table 2***: Summary of studies on ATAL aerosol composition using different models and
281   measurement techniques.

Study Method and Period	Aerosol Composition at the UTLS	Reference
Coupled Aerosol – Radiation – Earth System Model (2015, 2017, 2021)	Nitrate, Organics, Sulfate, Ammonium aerosols between 15°N–45°N and 0°E–160°E	Zhu et al. (2024)
Aircraft measurements	Nitrate, Ammonium, Sulfate, and Organic Carbon	Appel et al. (2022)

(2017)		
Offline ion chromatography (2017)	Nitrate and Nitrite aerosols	Vernier et al. (2022)
Earth System Model (2017 – 2021)	Nitrate (~30 – 40 %), Nitric Acid	Yu et al. (2022)
Earth System Model (2000 – 2015)	Sulfate (40%), secondary + primary organics (45%), Ammonium (14%), Trace (less than 3%) amount of BC	Bossolasco et al. (2021)
Chemical Transport Model (2013)	Organic Carbon, Nitrate, Sulfate, Ammonium	Fairlie et al. (2020)
Atmospheric Chemistry and General Circulation Model	Mineral Dust, Water Soluble (Sulfate and Nitrate) aerosols	Ma et al. (2019)
Satellite + Aircraft + Trajectory simulations + Cloud Chamber experiments (1997, 2002 – 2012, 2017)	Ammonium Nitrate	Hopfner et al. (2019)

282   To account for this variability, we considered seven UTLS aerosol scenarios with different

283   fractions of sulfate (SUL), nitrate (NIT), organic carbon (OC), and ammonium (AM), assuming

284   external mixing (**Table 3**). Among these scenarios, the OC-dominant combination (with 50% OC,

285   denoted as C1) and the combination with 40% OC and 30% AM (denoted as C2) are adapted,

286   respectively, from Bossolasco et al. (2021) and Appel et al. (2022). Two ideal scenarios are also

287   assumed where the sulfate and nitrate aerosols contribute 100% of the UTLS aerosols (SUL and

288   NIT, respectively). The SUL scenario serves as a reference, representing UTLS aerosols with

289   background sulfate levels similar to those in the stratosphere (Junge and Manson, 1961). The NIT

290   scenario defines an upper baseline, while the remaining cases (denoted as C1 to C5) explore

291   varying nitrate compositions from 0 to 0.4.

292 **Table 3:** Aerosol mixing scenarios considered for UTLS aerosols, with fractional compositions
293 (f_i) of sulfates (SUL), nitrates (NIT), organic carbon (OC), and ammonium sulfate (AM).

Combination	Fractional composition (f_i)			
	SUL	NIT	OC	AM
SUL	1	0	0	0
NIT	0	1	0	0
C1*	0.4	0	0.5	0.1
C2**	0.1	0.2	0.4	0.3
C3	0.2	0.3	0.3	0.2
C4	0.1	0.4	0.2	0.3
C5	0.2	0.3	0.1	0.4

294 ** This combination is adapted from Bossolasco et al. (2021)*

295 ***This combination is adapted from Appel et al. (2022)*

296 The SSA and ASY of each aerosol species were derived from their size distribution parameters

297 and complex refractive indices under dry conditions (**Table S2**) using the Mie scattering theory,

298 assuming that all the aerosol species follow the log-normal size distribution. If f_i is the fraction of

299 an individual aerosol species in a given combination, then SSA and ASY of the combination are

300 obtained using the following equations:

301
$$SSA(\lambda) = \frac{\sum_i f_i SSA_i(\lambda)}{\sum_i f_i} \qquad (7)$$

302
$$ASY(\lambda) = \frac{\sum_i f_i ASY_i(\lambda)}{\sum_i f_i} \qquad (8)$$

303 where SSAi and ASYi denote the single scattering albedo and asymmetry parameter of

304 respective aerosol species at a given wavelength λ. These derived SSA and ASY for each aerosol

305 combination at 455 and 940 nm are illustrated in **Figure 3**.

306 Among the compositions, the OC-dominant scenario (C1) exhibits the lowest SSA, indicating

307 higher absorption, while SSA increases with decreasing OC fractions and increasing fractions of

308   nitrates and ammonium (C2- C5). Sulfates and nitrates have SSA=1 at both wavelengths (445 nm

309   and 940 nm), with slight ASY differences (e.g., $ASY_{SUL} = 0.724$, $ASY_{NIT} = 0.718$ at 445 nm and

310    $ASY_{SUL} = 0.679$, $ASY_{NIT} = 0.549$ at 940 nm). These SSA and ASY values were applied to altitude

311   bins in the 10- to 20-km range.

312

313
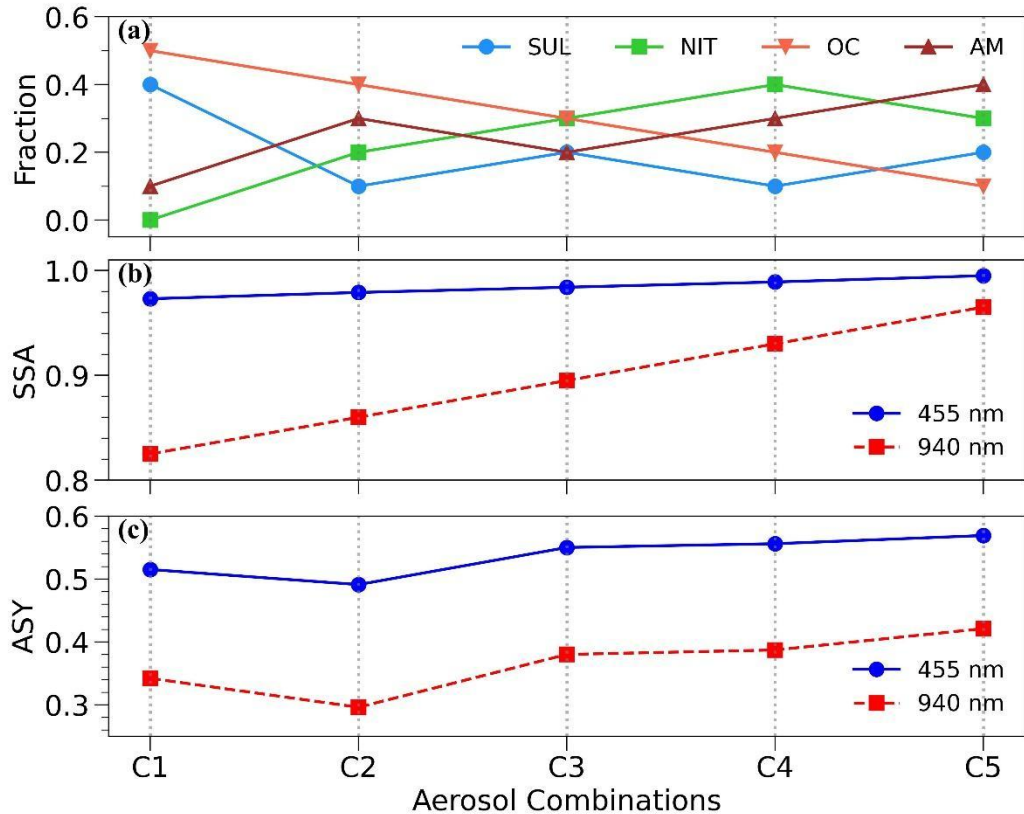
Figure 3: (a) Fractional contribution of aerosol species—sulfate (SUL), nitrate (NIT), organic
carbon (OC), and ammonium (AM)—in the aerosol mixing combinations (C1 to C5) considered
in this study. (b) Single Scattering Albedo (SSA) and (c) Asymmetry Parameter (ASY)
corresponding to each combination under dry conditions.

318   In the lower atmosphere (below 10 km), aerosol composition/typing was characterized using

319   seven-day air mass back trajectories at 500 m (boundary layer) and 4000 m (free troposphere)

320   above mean sea level, generated using the HYbrid Single Particle Lagrangian Integrated Trajectory

321   (HYSPLIT) model (Stein et al., 2015). Trajectories were clustered based on spatial similarity using

322   hierarchical clustering and the Total Spatial Variance (TSV) method, optimizing the number of

323   clusters where further TSV reduction provides minimal improvement. This approach identifies

324   distinct transport pathways shaped by synoptic-scale meteorology, allowing the classification of

325   aerosol types based on air mass origin, transport history, and residence time over source regions.

326   A similar approach was used by Pawar et al. (2015) in Pune to identify aerosol types through back

327   trajectory analysis. After categorizing the air-mass clusters based on potential aerosol types from

328   the Optical Properties of Aerosols and Clouds (OPAC) database (Hess et al., 1998; **Table S3**), the

329   corresponding wavelength and RH-dependent aerosol scattering properties (SSA and ASY) were

330   obtained. A detailed description of this method is provided in **Section S2** (Supplementary

331   Information) along with the identified aerosol types through back trajectory clusters at the three

332   locations for the two altitude levels (**Figure S4**). Since marine aerosols typically have a low scale

333   height (< 2 km), their influence was considered only within the boundary layer. Additionally, air

334   masses of oceanic origin that remained over land for more than 24 hours before arrival were

335   reclassified as continental aerosols.

336   **4.4. Radiative Transfer Calculations**

337   The radiative forcing due to aerosols at a given level of the atmosphere is the difference

338   between the radiative fluxes under aerosol-laden and no-aerosol (and without clouds) conditions.

339   For a given layer in the atmospheric column with its vertical thickness Δz (in km), this radiative

340   forcing (RF, in W m^{-2}) at its top and bottom levels is mathematically expressed as:

$$RF_{Top} = \left(F_{wa}^{\downarrow} - F_{wa}^{\uparrow}\right)_{Top} - \left(F_{na}^{\downarrow} - F_{na}^{\uparrow}\right)_{Top} \qquad (9)$$

$$RF_{Bot} = \left(F_{wa}^{\downarrow} - F_{wa}^{\uparrow}\right)_{Bot} - \left(F_{na}^{\downarrow} - F_{na}^{\uparrow}\right)_{Bot} \qquad (10)$$

343   Here, $F_{wa}^{\downarrow}$ and $F_{wa}^{\uparrow}$ represent the downward and upward radiative fluxes in aerosol-laden

344   conditions, while $F_{na}^{\downarrow}$ and $F_{na}^{\uparrow}$ denote the corresponding fluxes under no-aerosol (and without

345 clouds) conditions.

346 The Aerosol Radiative Forcing (ARF) of this atmospheric layer is the difference between the

347 RF at its top and bottom levels, which quantifies the amount of energy trapped within the layer

348 and represents the atmospheric absorption due to aerosols (Gadhavi and Jayaraman, 2006).

349 Mathematically,

$$ARF \equiv \Delta RF = RF_{Top} - RF_{Bot} \qquad (11)$$

350

351 The rate at which the atmosphere heats up due to aerosols (referred to as HR, in K day^{-1}) for a

352 given layer can be determined using the following equation (Liou, 2002):

$$HR = \frac{\partial T}{\partial t} = \frac{g}{C_p}\left(\frac{\Delta RF}{\Delta P}\right) = \frac{-1}{\rho C_p}\left(\frac{\Delta RF}{\Delta z}\right) \qquad (12)$$

353

354 In this equation, g represents the acceleration due to gravity, and C_p denotes the isobaric

355 specific heat capacity of dry air ($\sim$ 1006 J Kg^{-1} K^{-1}). ΔP signifies the pressure difference between

356 the top and bottom boundaries of the atmospheric layer, ρ indicates the density of the air (in kg m^{-3}

357 ^{3}), and $\Delta RF/\Delta z$ represents the radiative power absorbed or emitted by the medium per unit volume

358 of the atmosphere (in W m^{-3}). Since the atmosphere consists of several vertically heterogeneous

359 layers, repeating the above calculation for each layer yields the profile of the heating rate.

360 For estimating the radiative forcing and heating rates associated with UTLS aerosols, the

361 aerosol profiles (extinction coefficient, SSA, and ASY) and the atmospheric profiles (pressure,

362 temperature, water vapor density, and ozone density) are provided as input into the Santa Barbara

363 DISORT (discrete ordinate radiative transfer) Atmospheric Radiative Transfer (SBDART) model

364 (Ricchiazzi et al. 1998). This computational tool calculates plane-parallel radiative transfer in

365 various atmospheric and surface conditions, including clear and cloudy scenarios. The DISORT

366 module, which employs a numerically stable algorithm, is used to solve the equations of plane-

367 parallel radiative transfer in vertically inhomogeneous atmospheres (Stamnes et al., 1988). The

368 accuracy of the SBDART model is estimated to be within a few percent for clear-sky conditions.

369 The calculations are performed in the shortwave (SW) region (0.25–4 µm) with a spectral

370 resolution of 0.005 µm and 8 radiation streams at 1-h intervals for a range of solar zenith angles

371 to obtain a 24-hour average. Shortwave ARF is computed for both the atmospheric column

372 (extending from the surface at 0 km up to 30 km) and specifically for the UTLS region (12–20

373 km). Additionally, heating rate profiles are derived for the UTLS layer across all seven previously

374 discussed aerosol scenarios.

375 **5. Results and Discussions**

376 **5.1. Spatial Variability of ATAL Aerosols in the UTLS Region**

377 **Figure 4** presents the mean cloud-screened backscatter ratio at 455 nm (BSR455) for the UTLS

378 region over the study locations. The approximate vertical extent of the ATAL region is adapted

379 from Akhil Raj et al. (2022), where its boundaries are determined based on dynamic constraints.

380 The lower boundary corresponds to the convective outflow level, identified as the altitude where

381 the potential temperature gradient reaches a minimum below the cold point tropopause (CPT) after

382 applying a nine-point running mean. The upper boundary is defined by the altitude of maximum

383 stability (L_{maxS}), derived from the squared Brunt- Väisälä frequency (N^2). Their analysis indicates

384 that L_{maxS} is located 1–2.7 km above the CPT, corresponding to a potential temperature of

385 approximately 442.11 ± 25.64 K (454.39 ± 13.89 K) over the Indian region, roughly 19 km above

386 the Earth's surface. The convective outflow level, on the other hand, is observed at ~ 13 km across

387 all locations. Based on these criteria, we define the ATAL region's approximate vertical extent

388 between 13 km to 19 km, corresponding to a potential temperature range of 350 K to 440 K.

389 A consistent increase in aerosols is observed in the 16-18 km altitude range (365-400 K

390 potential temperature) across all study locations. The highest BSR455 values are recorded over

391 Varanasi and Hyderabad (~1.07), followed by Gadanki (~1.06), with site-specific variations in

392 backscatter profiles. These findings align with previous ATAL aerosol observations reported by

393 Akhil Raj et al. (2022). The maximum BSR_{455} value (1.07 over Varanasi) is comparable to that

394 observed over Nainital (29.35°N, 79.46°E) in August 2016 (Hanumanthu et al., 2020). For

395 reference, CALIPSO-derived BSR_{532} values for ATAL have been reported to range between 1.10

396 and 1.15, with an associated depolarization ratio of < 5% (Vernier et al., 2011), further supporting

397 the presence of submicron aerosols in this region.

398
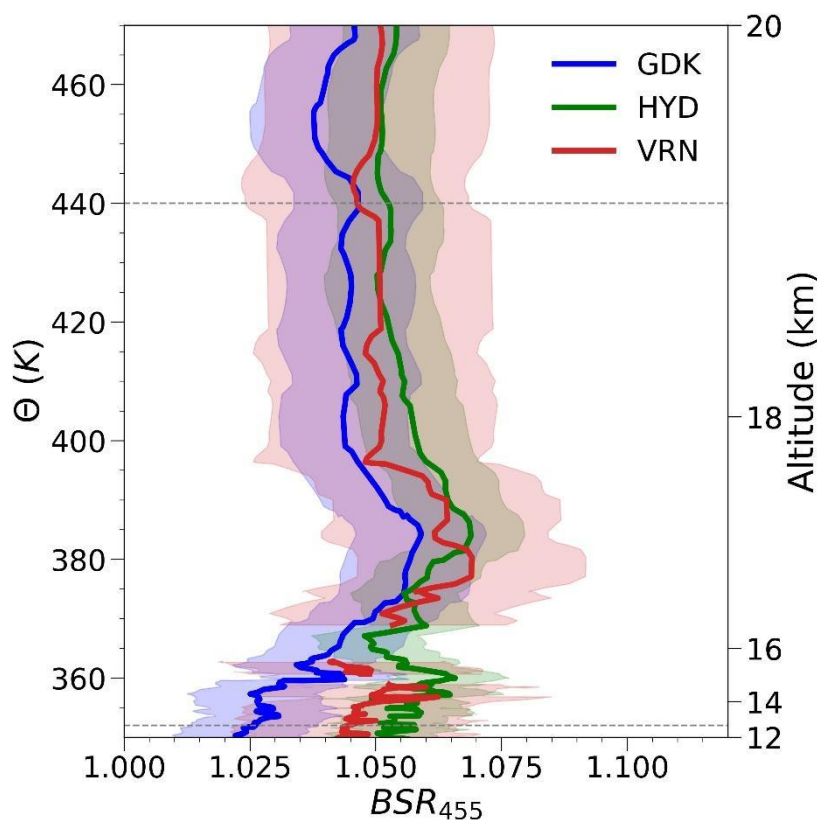
399 **Figure 4:** Mean cloud-screened backscatter ratios at 455 nm plotted against potential temperature
400 (Θ) on the primary y-axis and altitude on the secondary y-axis over Gadanki (GDK), Hyderabad
401 (HYD), and Varanasi (VRN). The dashed lines at 13 km and 19 km indicate the approximate
402 vertical extent of ATAL aerosols (see text for details).

403 Despite the observed enhancements, no clear monotonic trend in aerosol concentration

404 emerges across the study locations, which are positioned at different geographical points relative

405   to the ATAL core: Gadanki (southern periphery), Hyderabad (transition region), and Varanasi

406   (central ATAL region). However, the slightly lower aerosol BSR at Gadanki suggests a weaker

407   ATAL influence at the outermost edge. Further validation through extensive in-situ and satellite-

408   based observations is necessary to confirm these spatial trends and understand the seasonal and

409   inter-annual variability of ATAL aerosols.

410   **5.2. Impact of UTLS Aerosol Composition on Radiative Forcing and its Contribution to the**

411   **Atmospheric Column**

412   **Figure 5(a)** illustrates the ARF in the UTLS region, which exhibits a net positive forcing

413   (warming) across all aerosol combinations. However, under sulfate- and nitrate-dominant

414   scenarios (SUL and NIT, respectively), the warming effect is negligible (<0.02 W m^{-2}) across all

415   locations. In contrast, mixed aerosol scenarios (C1–C5) display a stronger UTLS forcing, ranging

416   from 0.06 to 0.23 W m^{-2} over Gadanki, 0.06 to 0.29 W m^{-2} over Hyderabad, and 0.07 to 0.29 W

417   m^{-2} over Varanasi. Similar magnitudes are observed in Hyderabad and Varanasi, with slightly

418   lower values over Gadanki, indicating a spatial variability in UTLS absorption. Among the mixed

419   aerosol scenarios, the OC-dominant case (C1) exhibits the highest UTLS absorption, whereas C5,

420   where organic carbon (OC) contributes only 10% and ammonium and nitrate dominate (70%),

421   shows the lowest absorption. The successive decrease in UTLS absorption from C1 to C5

422   highlights the role of absorbing aerosols in enhancing radiative warming in the UTLS. Considering

423   the estimates using previously reported aerosol compositions (C1 from Bossolasco et al., 2021 and

424   C2 from Appel et al., 2022), the UTLS forcing ranged from 0.19 to 0.29 W m^{-2} across different

425   locations.

426   When considering the total aerosol radiative forcing (ARF$_{ATM}$), the highest values are observed

427   over Varanasi (up to 22.5 W m^{-2}), followed by Hyderabad (up to 16.4 W m^{-2}) and Gadanki (up to

428   8.92 W m^{-2}) (**Fig. 5(b)**). Since these forcing results from aerosols across multiple atmospheric

429   layers, the UTLS contribution is quantified in terms of the percent fraction of the total ARF (**Fig.**

430   **5(c)**). The OC-dominant scenario (C1) exhibits the highest relative UTLS contribution (up to

431   2.7%), with a decreasing trend as the OC fraction is reduced (C2–C5), consistent with the ARF$_{UTLS}$

432   variations discussed earlier. In sulfate- and nitrate-dominant cases (SUL and NIT), the UTLS

433   contribution is minimal (0.1%).

434

435
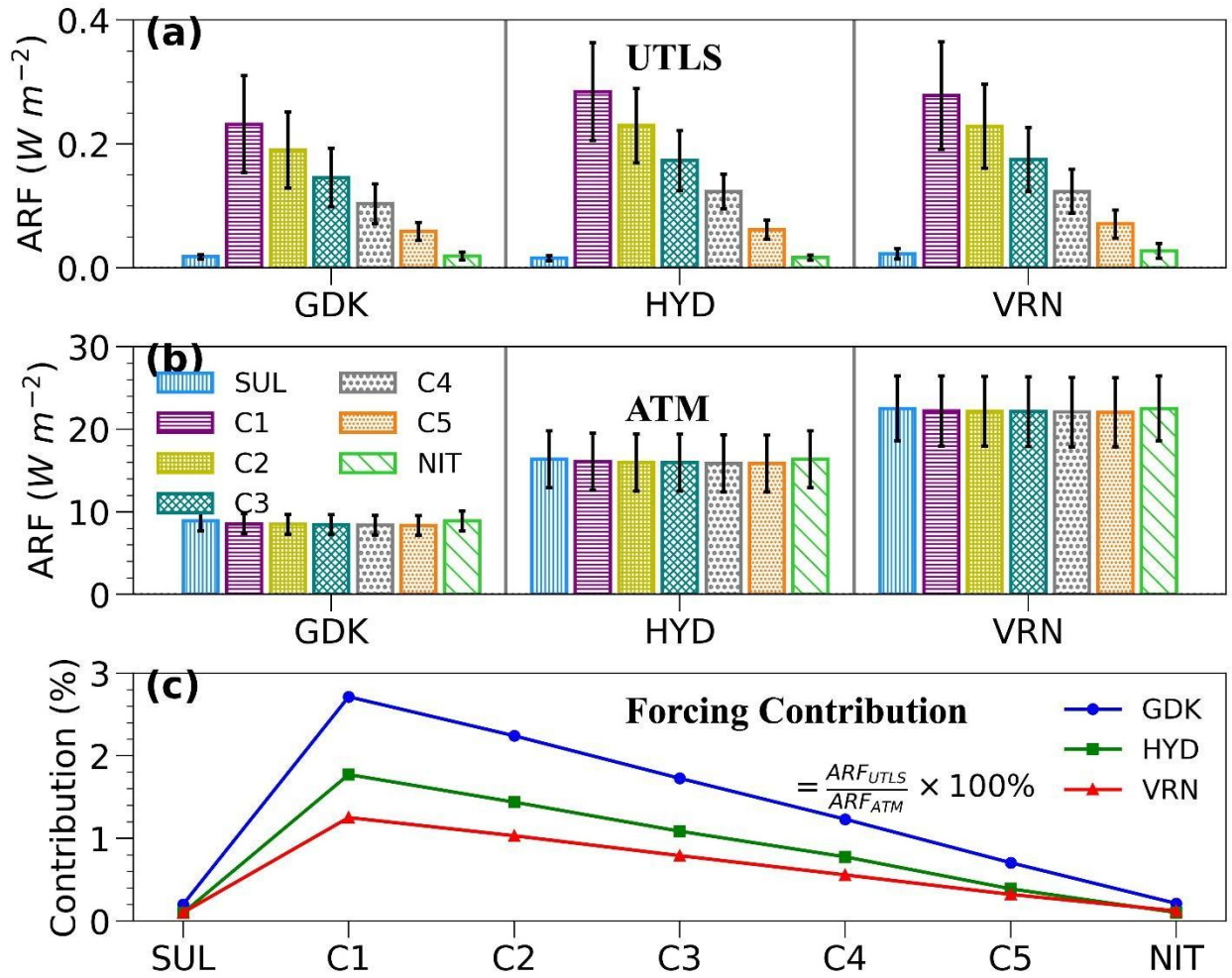
Figure 5: Aerosol Radiative Forcing (ARF) for different aerosol scenarios in the UTLS region over Gadanki (GDK), Hyderabad (HYD), and Varanasi (VRN) during the study period: (a) ARF in the UTLS region, (b) ARF in the total atmospheric column from the surface to 30 km, and (c) percent fractional contribution of UTLS forcing to the total atmospheric forcing.

The variation in UTLS forcing contribution across study locations suggests differences in the overall aerosol distribution within the atmospheric column. Despite similar absolute UTLS forcing values, its relative contribution is highest over Gadanki, moderate over Hyderabad, and lowest over Varanasi. This pattern suggests that over Varanasi, the dominant contribution to atmospheric absorption comes from aerosols in the lower atmosphere, likely driven by the presence of strongly absorbing aerosols in this location (**Table S3**). Conversely, at Gadanki, the lower atmosphere appears to be dominated by scattering aerosols, resulting in reduced absorption, which increases

447 the relative importance of UTLS forcing. These findings underscore the significant impact of lower

448 atmospheric aerosol composition on the contribution of UTLS aerosols to total atmospheric

449 forcing at various locations.

450   To quantify the influence of aerosol composition on radiative forcing in the UTLS, we

451 examined the difference in radiative forcing (δARF) between various aerosol scenarios and a

452 sulfate-dominant (SUL) reference case. The δARF was computed as:

453 $$\delta ARF_x = ARF_x - ARF_{SUL} \qquad (13)$$

454   where x represents the mixed-aerosol compositions (C1 to C5) and nitrate-dominant (NIT)

455 composition. The sign of δARF_x indicates whether a given aerosol composition induces further

456 warming or cooling in the UTLS and the atmospheric column relative to the sulfate baseline.

457   In the UTLS, δARF_x values are predominantly positive, suggesting that all tested aerosol

458 compositions—except the nitrate-dominant (NIT) case—contribute to warming (**Fig. 6a**). The

459 δARF for the NIT scenario remains close to zero across all locations, implying minimal radiative

460 influence from nitrate aerosols in the UTLS. The magnitude of δARF_x varies significantly, ranging

461 from 0.06 to 0.28 W m^{-2} (an increase of 300–1400%) over Varanasi, 0.05 to 0.27 W m^{-2} (250–

462 1300%) over Hyderabad, and 0.03 to 0.2 W m^{-2} (150–1000%) over Gadanki. These large

463 variations highlight the strong sensitivity of UTLS radiative forcing to aerosol composition, where

464 even small changes in aerosol properties result in disproportionately large changes in forcing.
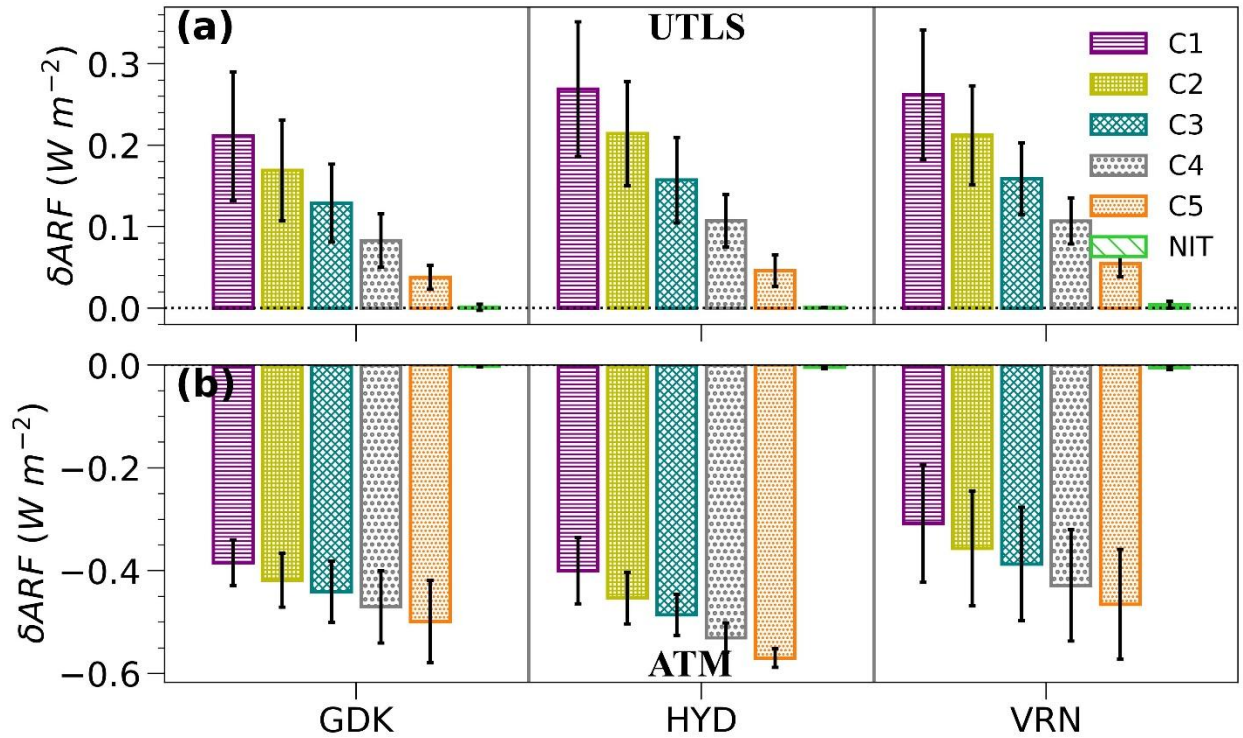
Figure 6: Differences in Aerosol Radiative Forcing (δARF) due to changes in aerosol composition within the UTLS region, with sulfate forcing as the reference ($\delta ARF_x = ARF_x - ARF_{SUL}$, where 'x' represents NIT and C1 to C5): (a) δARF in the UTLS region and (b) δARF for the entire atmospheric column.

Among the mixed compositions (C1-C5), the largest δARF_x occurs in the OC-dominant scenario (C1) (Bossolasco et al., 2021), highlighting the strong absorptive nature of organic carbon in the UTLS. A progressive reduction in δARF is observed with decreasing OC fraction and increasing nitrate and ammonium content (C2 to C5), indicating that absorbing aerosols, such as OC, substantially modify the UTLS radiative forcing. In the atmospheric column, δARF_{ATM} values are negative, indicating that changes in UTLS aerosol composition led to a decrease in atmospheric forcing (**Fig. 6b**). The magnitudes of δARF_{ATM} reach approximately -0.5 W m^{-2} (5%) over Gadanki, -0.6 W m^{-2} (4%) over Hyderabad, and -0.5 W m^{-2} (2.3%) over Varanasi. This suggests that while UTLS aerosol composition significantly alters radiative forcing at high altitudes, the net effect on the entire atmospheric column remains relatively modest.

5.3. Influence of Aerosol Composition on Heating Rates in the UTLS

Shortwave heating rates associated with mixed-type aerosol compositions in the UTLS (C1 to C5) are significantly higher than those observed under sulfate- (SUL) and nitrate-dominant (NIT) scenarios (**Fig. 7**). Neither the SUL nor NIT cases exhibit distinct heating rate patterns at ATAL altitudes, with only slight warming observed, peaking at approximately 0.003 K day^{-1}. This negligible difference between sulfate and nitrate aerosols can be attributed to their similar optical properties, as discussed in Santhosh et al. (2025). In contrast, enhanced heating rates are observed between 16–18 km (365–404 K potential temperature) over Gadanki, 14–16 km (357–366 K) over Hyderabad, and 16–18 km (367–403 K) over Varanasi for the mixed aerosol scenarios (C1 to C5). The heating in the ATAL layer reaches a maximum of 0.03 K day^{-1}, with Varanasi exhibiting notably higher heating rates than the other locations.

Consistent with the discussion on UTLS radiative forcing, the highest heating rates occur in the OC-dominant composition (C1). A progressive decline is observed as the OC fraction decreases while ammonium and nitrate fractions increase (C2 to C5). These results highlight the warming effect of absorbing aerosols in the UTLS. Previous studies, such as Fadnavis et al. (2022), reported UTLS warming due to anthropogenic aerosols, with estimates ranging from 0.02 to 0.3 K per month, equivalent to an upper limit of ~0.01 K day^{-1}. Similarly, carbonaceous aerosols with strong absorption characteristics have been shown to increase UTLS heating by 0.001 to 0.02 K day^{-1} (Chavan et al., 2021).

499
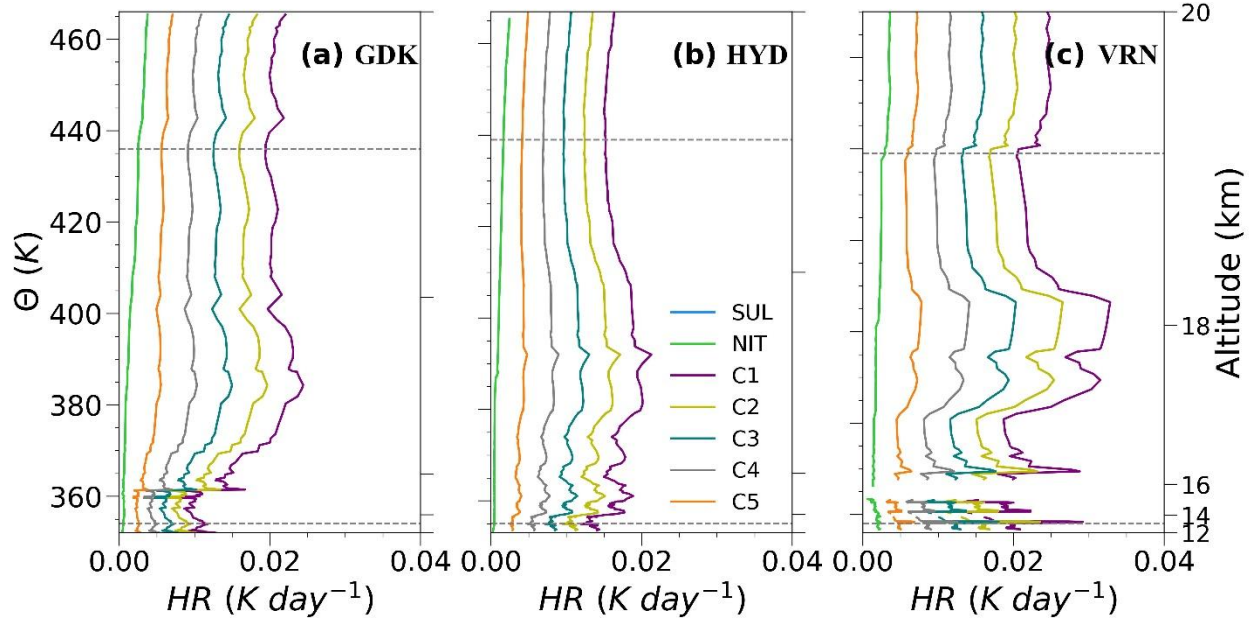
Figure 7: Aerosol heating rates in the UTLS plotted against potential temperature (Θ) and altitude over (a) Gadanki, (b) Hyderabad, and (c) Varanasi. The gray dashed lines at 13 km and 19 km indicate the approximate vertical extent of ATAL.

To evaluate the sensitivity of heating rates to changes in aerosol composition within the ATAL region, we estimate the difference in heating rates (δHR) for the nitrate (NIT) and mixed-aerosol compositions (C1–C5) relative to the sulfate (SUL) reference scenario across 13–19 km as:

$$\delta HR_x = HR_x - HR_{SUL} \qquad (14)$$

where *x* represents aerosol compositions other than sulfates. The δHR values range from ~0 to 0.03 K day^{-1} across the locations (**Fig. 8**).
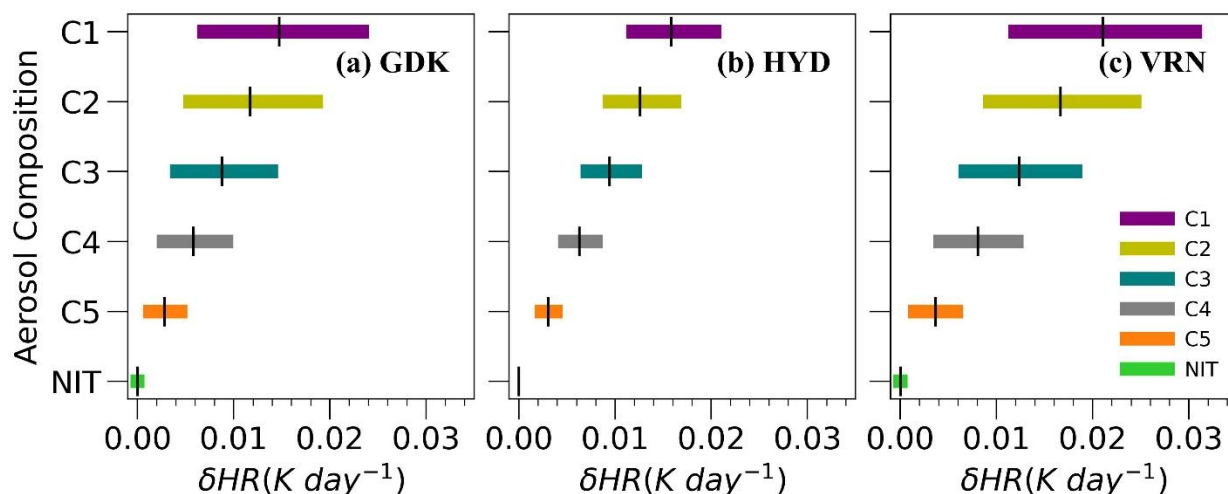
Figure 8: Range of changes in aerosol heating rates due to different aerosol compositions relative to the sulfate-dominant scenario ($\delta HR = HR_x - HR_{SUL}$, where 'x' represents compositions other than sulfates) over (a) Gadanki (GDK), (b) Hyderabad (HYD), and (c) Varanasi (VRN). Horizontal bars represent the minimum-to-maximum range of δHR, while small black vertical markers indicate the mean values.

A broader range of δHR is observed for compositions with a higher OC fraction, such as C1 (50% OC) and C2 (40% OC), leading to heating rate increases from 0.01 to 0.03 K day^{-1}, which is approximately 10–30 times larger than the sulfate baseline. As the OC fraction decreases, the δHR range also diminishes, similar to the δARF trend discussed earlier. Due to the comparable heating rates of nitrate and sulfate aerosols in the UTLS, the δHR associated with the NIT scenario remains negligible. However, when nitrates constitute a significant portion of the mixed compositions (e.g., 30% in C5 and 40% in C4), along with ammonium aerosols (40% in C5 and 30% in C4), δHR values become non-negligible (~0.001 to 0.01 K day^{-1}), leading to a 10-fold increase in heating rates compared to the sulfate reference. These results confirm that variations in aerosol composition in the UTLS have a substantial impact on heating rates, further influencing radiative effects and atmospheric stability in this region.

5.4. Comparison of Heating Rates at Point Locations Relative to Spatially Averaged Estimates

Since this study focuses on heating rates at specific point locations, it is valuable to compare these estimates with those obtained for a broader spatial domain using a similar methodology. A recent study by Santhosh et al. (2025) examined radiative forcing and heating rates in the 12–20 km altitude range over a broader geographic region within the Asian Summer Monsoon Anticyclone (ASMA) (25°N–37.5°N, 40°E–95°E) using Cloud-Aerosol Lidar with Orthogonal Polarization (CALIOP) data. In that study, three dominant aerosol scenarios were considered in the UTLS: sulfate, nitrate, and anthropogenic aerosols. The sulfate and nitrate aerosols had microphysical properties similar to those in our study, while the anthropogenic aerosol model was based on the continental clean aerosol model of Hess et al. (1998), representing a mixed-aerosol scenario.

To assess the representativeness of the point-location heating rates, we compare the sulfate- and nitrate-dominated cases from the present study with the corresponding heating rates reported by Santhosh et al. (2025). Although a direct comparison of mixed aerosols is more complex due to differences in aerosol definitions, we use the composition with the highest heating rates from this study (C1) as a reference for comparison against the anthropogenic heating rates reported by Santhosh et al. (2025).

Our analysis reveals that heating rates at individual locations (Gadanki, Hyderabad, and Varanasi) are slightly higher than the spatially averaged heating rates over the ASMA region under sulfate- and nitrate-dominant scenarios (**Fig. 9**). However, for the mixed-aerosol scenarios, the

548 heating rates estimated over the ASMA region exceed those observed at individual point locations.

549
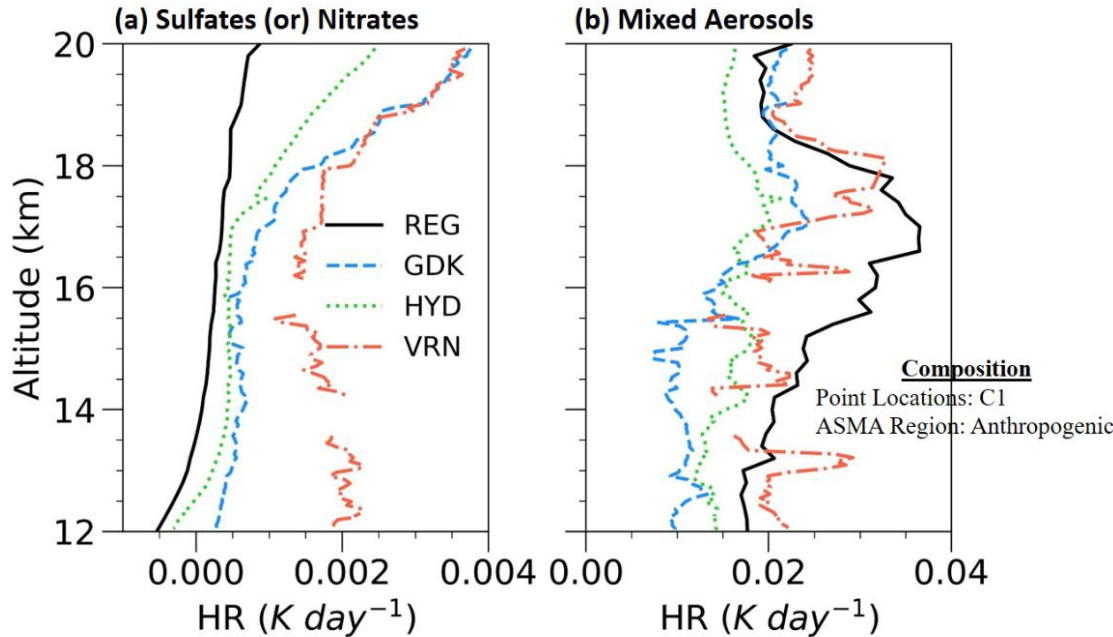
Figure 9: Comparison of UTLS heating rates for (a) sulfate or nitrate-dominant composition and (b) mixed aerosol composition across the UTLS region (REG: 25°N–37.5°N, 40°E–95°E, adapted from Santhosh et al. (2025)), as well as over Gadanki (GDK), Hyderabad (HYD), and Varanasi (VRN). In the mixed aerosol scenario, the composition with the highest observed heating rates (C1) is compared with the anthropogenic composition in the UTLS region reported by Santhosh et al. (2025). As Santhosh et al. (2025) also observed a near-similar heating rate pattern for sulfates and nitrates, consistent with the present study, only heating rates with nitrates are plotted here.

557 This discrepancy can be attributed to the interplay between aerosol optical properties and

558 spatial averaging effects. Santhosh et al. (2025) assumed that the climatological mean and standard

559 deviation profiles of aerosol backscatter ratios sufficiently capture the spatial heterogeneity of

560 ATAL in radiative transfer calculations. Scattering aerosols, such as sulfates and nitrates, primarily

561 reflect shortwave radiation and do not significantly contribute to global warming or atmospheric

562 heating. When averaged over a large spatial domain, the weak radiative response of these aerosols

563 is integrated across a broader region, leading to lower overall heating rates.

564   In contrast, the heating effects of absorbing aerosols within mixed-aerosol scenarios are less

565   sensitive to spatial heterogeneity. Even small fractions of absorbing aerosols in the ATAL

566   contribute to warming, and regional averaging enhances this consistent heating effect. This

567   explains why the ASMA-wide mixed-aerosol heating rates exceed those at point locations. These

568   findings suggest that the mixed-aerosol compositions considered in this study may lead to stronger

569   warming in the UTLS over a broader spatial domain. Further investigations with realistic

570   observational constraints and model validation are needed to better quantify these effects.

571   **6. Summary and Conclusions**

572   This study presents a detailed analysis of the shortwave radiative impacts of monsoon UTLS

573   aerosols, focusing on radiative forcing and heating rates derived from balloon-borne in situ

574   measurements conducted as part of the Balloon Measurement Campaigns of the Asian Tropopause

575   Aerosol Layer (BATAL) between 2014 and 2018. To assess aerosol effects, we considered seven

576   aerosol compositions dominated by different species: (i) sulfate (SUL), representing the

577   background or reference condition, (ii) nitrate (NIT), a primarily scattering aerosol, and (iii) five

578   mixed-type aerosol scenarios incorporating varying fractions of sulfates, nitrates, organic carbon,

579   and ammonium aerosols. The key findings from this study, based on measurements at Gadanki,

580   Hyderabad, and Varanasi, are summarized as follows:

581   (i)   **Aerosol Enhancement in ATAL Altitudes**: A significant enhancement in aerosol

582   backscatter was observed in the 13–19 km altitude range across all locations, with

583   BSR455 peaks reaching up to 1.07 over Varanasi and Hyderabad and 1.06 over Gadanki.

584   (ii)   **UTLS Radiative Forcing and its contribution to total atmospheric forcing:** A net

585   positive aerosol forcing was observed in the UTLS region, contributing between 0.1%

586   and 3% of the total atmospheric column forcing. Among the tested compositions, the

587   scenario with 50% organic carbon (C1) exhibited the highest contribution (1.25%–3%),

588   whereas nitrate- and sulfate-dominated scenarios contributed significantly less (0.1%–

589   0.2%). The highest UTLS forcing estimates were recorded over Varanasi and

590   Hyderabad (~0.3 W m^{-2}), followed by Gadanki (0.23 W m^{-2}). Under sulfate- and nitrate-

591   dominant conditions, forcing remained nearly uniform across locations, with values not

592   exceeding 0.02 W m^{-2}. The UTLS forcing decreased with increasing fractions of nitrate

593   and ammonium.

594   (iii)   **Heating Rates in the UTLS Region:** The heating rate profiles for mixed-aerosol

595   compositions exhibited a notable increase in aerosol-induced heating at ATAL altitudes,

596   with rates reaching up to 0.03 K day^{-1} across the study locations. However, heating rates

597   for sulfate- and nitrate-dominant scenarios were approximately one-tenth of those

598   observed under mixed-aerosol conditions, suggesting significantly weaker or negligible

599   heating.

600   (iv) **Influence of the UTLS aerosol composition on the radiative forcing and heating**

601   **rates:** To quantify the impact of aerosol composition on radiative forcing, we used the

602   sulfate-dominant scenario as a reference. While replacing sulfates with nitrates led to

603   minimal changes in radiative forcing, the inclusion of organic carbon and ammonium in

604   mixed-aerosol compositions resulted in disproportionate increases in UTLS radiative

605   forcing (up to 14-fold). However, in terms of total column atmospheric forcing, these

606   changes were relatively modest, with a maximum reduction of ~5%, underscoring the

607   localized nature of UTLS radiative effects. Heating rate variations followed a similar

608   pattern, with mixed-aerosol scenarios exhibiting up to a 30-fold increase compared to

609   sulfate-dominated conditions.

610   (v)   **Comparison with Spatially Averaged UTLS Heating Rates:** When comparing our

611   point-location heating rate estimates with spatially averaged heating rates over the

612   ASMA region (Santhosh et al., 2025), we found that mixed absorbing and scattering

613   aerosols produced a stronger regional warming effect, whereas purely scattering

614   aerosols (e.g., sulfates, nitrates) had a weaker impact. This suggests that regional-scale

615   radiative effects are more sensitive to variations in ATAL aerosol composition.

616   Although this study considered near-realistic aerosol compositions for the ATAL, the actual

617 chemical composition of UTLS aerosols remains a challenge due to spatial and temporal variability

618 (Hanumanthu et al., 2020). Observational datasets with altitude-resolved aerosol composition are

619 essential for improving radiative impact assessments. Additionally, while dust and black carbon

620 have been detected in the ATAL (Bossolasco et al., 2021; Ma et al., 2019), previous studies have

621 shown that dust has minimal impact on clear-sky shortwave heating rates (Gao et al., 2023), and

622 black carbon concentrations are modest in the ATAL, as indicated by recent in situ measurements

623 (Appel et al., 2022; Vernier et al., 2022). Therefore, these species were excluded from our analysis.

624   A significant limitation of the study is its reliance on shortwave radiative effects, as nitrate

625 and sulfate aerosols exhibit similar scattering properties across the shortwave spectrum. However,

626 nitrates have distinct absorption features in the thermal infrared, which could influence longwave

627 radiative forcing. Future studies should incorporate improved measurements in the longwave and

628 thermal infrared regions to assess the full radiative impact of nitrate aerosols. Additionally, given

629 the sensitivity of UTLS radiative effects to water vapor concentrations (Santhosh et al., 2024a),

630 further investigations are necessary to assess the coupled effects of aerosols and water vapor on

631 the UTLS radiative balance.

632   Given the geographic and temporal limitations of in-situ observations, an integrated approach

633   combining satellite retrievals, reanalysis datasets, and in-situ measurements is crucial for tracking

634   long-term trends in ATAL radiative forcing and heating rates. Ongoing efforts in this direction are

635   expected to refine our understanding of the effects of UTLS aerosols. One of the key questions

636   that remains unexplored is whether the ATAL aerosol's chemical composition has any role in

637   strengthening or weakening the monsoon anticyclone. By modulating radiative heating, aerosols

638   can influence the temperature gradient and stability of the upper troposphere, potentially altering

639   the strength and persistence of the anticyclonic circulation. Finally, the second phase of BATAL,

640   which commenced in August 2024, is anticipated to yield new insights into ATAL composition

641   and radiative effects, particularly regarding the impact of wildfires and volcanic eruptions. These

642   findings will be instrumental in refining the understanding of UTLS aerosol-radiation interactions.

Code/Data availability

644   The data collected from the BATAL campaigns is available on request.

Author contribution

646   **V.N. Santhosh:** Data curation, Formal analysis, Investigation, Software, Validation,
647   Visualization, Writing – original draft. **B.L. Madhavan:** Conceptualization, Investigation,
648   Methodology, Supervision, Writing – review & editing. **S.T. Akhil Raj:** Data curation,
649   Visualization, Writing – review & editing. **M. Venkat Ratnam:** Supervision, Project
650   administration, Resources, Writing – review & editing. **J-P. Vernier:** Project administration,
651   Resources, Writing – review & editing. **F.G. Wienhold:** Software, Writing – review & editing.

Competing interests

653   The authors declare that they have no conflict of interest.

Acknowledgements

The findings presented in this paper are derived from the ISRO-NASA joint BATAL campaign, which was supported by the National Atmospheric Research Laboratory (NARL) under the Department of Space (DoS) and NASA ROSES Upper Atmospheric Research Program and Atmospheric Composition Modeling and Analysis Program (UARP, ACMAP, UACO). We extend our gratitude and acknowledge Dr. Amit Kumar Pandit, National Institute of Aerospace, Hampton, USA, and other members from NARL Gadanki, TIFR Balloon Facility, Hyderabad, and BHU Varanasi for their active involvement in the BATAL project from Gadanki to Varanasi. We thank NASA's Earthdata team for providing free access to their MERRA-2, MODIS, MLS, and AIRS datasets, which were used as supportive data in this study. We also thank the National Oceanic and Atmospheric Administration (NOAA)'s Air Resources Laboratory (ARL) for their HYSPLIT software.

References

Akhil Raj, S. T., Venkat Ratnam, M., Narayana Rao, D., and Krishna Murthy, B. V.: Vertical distribution of ozone over a tropical station: Seasonal variation and comparison with satellite (MLS, SABER) and ERA-Interim products, Atmos. Environ., 116, 281–292, https://doi.org/10.1016/j.atmosenv.2015.06.047, 2015.

Akhil Raj, S. T., Ratnam, M. V., Vernier, J. P., Pandit, A. K., and Wienhold, F. G.: Defining the upper boundary of the Asian Tropopause Aerosol Layer (ATAL) using the static stability, Atmos. Pollut. Res., 13(6), 101451, https://doi.org/10.1016/j.apr.2022.101451, 2022.

Angstrom, A.: Technique of determining the turbidity of the atmosphere, Tellus, 13(2), 214-223, https://doi.org/10.1111/j.2153-3490.1961.tb00078.x, 1964.

Appel, O., Köllner, F., Dragoneas, A., Hünig, A., Molleker, S., Schlager, H., Mahnke, C., Weigel, R., Port, M., Schulz, C., Drewnick, F., Vogel, B., Stroh, F., and Borrmann, S.: Chemical analysis of the Asian tropause aerosol layer (ATAL) with emphasis on secondary aerosol particles using aircraft-based in situ aerosol mass spectrometry, Atmos. Chem. Phys., 22(20), 13607–13630, https://doi.org/10.5194/acp-22-13607-2022, 2022.

Basha, G., Ratnam, M. V., Jiang, J. H., Kishore, P., and Babu, S. R.: Influence of indian summer monsoon on tropopause, trace gases and aerosols in Asian summer monsoon anticyclone observed by COSMIC, MLS and CALIPSO, Remote Sens., 13(17), https://doi.org/10.3390/rs13173486, 2021.

Bossolasco, A., Jegou, F., Sellitto, P., Berthet, G., Kloss, C., and Legras, B.: Global modeling studies of composition and decadal trends of the Asian Tropopause Aerosol Layer, Atmos. Chem. Phys., 21(4), 2745–2764, https://doi.org/10.5194/acp-21-2745-2021, 2021.

Chavan, P., Fadnavis, S., Chakroborty, T., Sioris, C. E., Griessbach, S., and Müller, R.: The outflow of Asian biomass burning carbonaceous aerosol into the upper troposphere and lower

stratosphere in spring: Radiative effects seen in a global model, Atmos. Chem. Phys., 21(18), 14371–14384, https://doi.org/10.5194/acp-21-14371-2021, 2021.

Che, H., Gui, K., Xia, X., Wang, Y., Holben, B. N., Goloub, P., Cuevas-Agulló, E., Wang, H., Zheng, Y., Zhao, H., and Zhang, X.: Large contribution of meteorological factors to inter-decadal changes in regional aerosol optical depth, Atmos. Chem. Phys., 19(16), 10497–10523, https://doi.org/10.5194/acp-19-10497-2019, 2019

Collis, R. T. H. and Russell, P. B.: Lidar Measurement of particles and gases by elastic backscattering and differential absorption, in: Laser Monitoring of the Atmosphere, edited by: Hinkley, E. D., Springer Verlag, Berlin, Germany, 71-151, https://doi.org/10.1007/3-540-07743-X_18, 2005.

Fadnavis, S., Chavan, P., Joshi, A., Sonbawne, S. M., Acharya, A., Devara, P. C. S., Rap, A., Ploeger, F., and Müller, R.: Tropospheric warming over the northern Indian Ocean caused by South Asian anthropogenic aerosols: Possible impact on the upper troposphere and lower stratosphere, Atmos. Chem. Phys., 22(11), 7179–7191, https://doi.org/10.5194/acp-22-7179-2022, 2022.

Fadnavis, S., Semeniuk, K., Pozzoli, L., Schultz, M. G., Ghude, S. D., Das, S., and Kakatkar, R.: Transport of aerosols into the UTLS and their impact on the Asian monsoon region as seen in a global model simulation, Atmos. Chem. Phys., 13(17), 8771–8786, https://doi.org/10.5194/acp-13-8771-2013, 2013.

Fairlie, T. D., Liu, H., Vernier, J. P., Campuzano-Jost, P., Jimenez, J. L., Jo, D. S., Zhang, B., Natarajan, M., Avery, M. A., and Huey, G.: Estimates of Regional Source Contributions to the Asian Tropopause Aerosol Layer Using a Chemical Transport Model, J. Geophys. Res.-Atmos., 125(4), 1–20, https://doi.org/10.1029/2019JD031506, 2020.

Gadhavi, H. and Jayaraman, A.: Airborne lidar study of the vertical distribution of aerosols over Hyderabad, an urban site in central India, and its implication for radiative forcing calculations, *Ann. Geophys.*, 24, 2461–2470, https://doi.org/10.5194/angeo-24-2461-2006, 2006.

Gao, J., Huang, Y., Peng, Y., and Wright, J. S.: Aerosol Effects on Clear-Sky Shortwave Heating in the Asian Monsoon Tropopause Layer, J. Geophys. Res.-Atmos., 128(4), 1–23, https://doi.org/10.1029/2022JD036956, 2023.

Gupta, G., Ratnam, M. V., Madhavan, B. L., Prasad, P., and Narayanamurthy, C. S.: Vertical and spatial distribution of elevated aerosol layers obtained using long-term ground-based and space-borne lidar observations, Atmos. Environ., 246, 118172. https://doi.org/10.1016/j.atmosenv.2020.118172, 2021.

Hanumanthu, S., Vogel, B., Müller, R., Brunamonti, S., Fadnavis, S., Li, D., Ölsner, P., Naja, M., Singh, B. B., Kumar, K. R., Sonbawne, S., Jauhiainen, H., Vömel, H., Luo, B., Jorge, T.,

Wienhold, F. G., Dirkson, R., and Peter, T.: Strong day-to-day variability of the Asian Tropopause Aerosol Layer (ATAL) in August 2016 at the Himalayan foothills, Atmos. Chem. Phys., 20(22), 14273–14302, https://doi.org/10.5194/acp-20-14273-2020, 2020.

He, Q., Ma, J., Zheng, X., Wang, Y., Wang, Y., Mu, H., Cheng, T., He, R., Huang, G., Liu, D., and Lelieveld, J.: Formation and dissipation dynamics of the Asian tropopause aerosol layer, Environ. Res. Letts., 16(1), https://doi.org/10.1088/1748-9326/abcd5d, 2020.

Hess, M., Koepke, P., and Schult, I.: Optical Properties of Aerosols and Clouds: The Software Package OPAC, Bull. Am. Meteorol. Soc., 79(5), 831–844, https://doi.org/10.1175/1520-0477(1998)079<0831:OPOAAC>2.0.CO;2, 1998.

Höpfner, M., Ungermann, J., Borrmann, S. et al.: Ammonium nitrate particles formed in upper troposphere from ground ammonia sources during Asian monsoons, Nat. Geosci., 12(8), 608–612, https://doi.org/10.1038/s41561-019-0385-8, 2019.

Junge, C. E. and Manson, J. E.: Stratospheric aerosol studies, *J. Geophys. Res.*, 66, 7, 2163–2182, https://doi.org/10.1029/JZ066i007p02163, 1961.

Komhyr, W. D., Barnes, R. A., Brothers, G. B., Lathrop, J. A., and Opperman, D. P.: Electrochemical concentration cell ozonesonde performance evaluation during STOIC 1989, J. Geophys. Res., (D5), 9231–9244, https://doi.org/10.1029/94JD02175, 1995.

Kumar, A. H., and Ratnam, M. V.: Variability in the UTLS chemical composition during different modes of the Asian Summer Monsoon Anti-cyclone, Atmos. Res., 260, 105700, https://doi.org/10.1016/j.atmosres.2021.105700, 2021.

Lau, W. K. M., Yuan, C., and Li, Z.: Origin, Maintenance and Variability of the Asian Tropopause Aerosol Layer (ATAL): The Roles of Monsoon Dynamics, Sci. Rep., 8(1), 1–14, https://doi.org/10.1038/s41598-018-22267-z, 2018.

Lelieveld, J., Bourtsoukidis, E., Brühl, C., Fischer, H., Fuchs, H., Harder, H., Hofzumahaus, A., Holland, F., Marno, D., Neumaier, M., Pozzer, A., Schlager, H., Williams, J., Zahn, A., & Ziereis, H.: The South Asian monsoon—Pollution pump and purifier. *Science*, *361*(6399), 270–273. https://doi.org/10.1126/science.aar2501, 2018.

Liou, K. N.: An Introduction to Atmospheric Radiation, 2nd Edition, Academic Press, Cambridge, MA, USA, 1053 pp., ISBN 9780123958259, 2002.

Ma, J., Brühl, C., He, Q., Steil, B., Karydis, V. A., Klingmüller, K., Tost, H., Chen, B., Jin, Y., Liu, N., Xu, X., Yan, P., Zhou, X., Abdelrahman, K., Pozzer, A., and Lelieveld, J.: Modeling the aerosol chemical composition of the tropopause over the Tibetan Plateau during the Asian summer monsoon, Atmos. Chem. Phys., 19(17), 11587–11612, https://doi.org/10.5194/acp-19-11587-2019, 2019.

761 Madhavan, B. L., Krishnaveni, A. S., Ratnam, M. V., and Ravi Kiran, V.: Climatological aspects
762   of size-resolved column aerosol optical properties over a rural site in the southern peninsular
763   India, Atmos. Res., 249, 105345, https://doi.org/10.1016/j.atmosres.2020.105345, 2021.

764 Miloshevich, L. M., Vömel, H., Whiteman, D. N., Lesht, B. M., Schmidlin, F. J., and Russo, F.:
765   Absolute accuracy of water vapor measurements from six operational radiosonde types
766   launched during AWEX-G, and implications for AIRS validation, *J. Geophys. Res.*, **111**,
767   D09S10, https://doi.org/10.1029/2005JD006083, 2006.

768 Murari, V., Kumar, M., Mhawish, A., Barman, S. C., and Banerjee, T.: Airborne particulate in
769   Varanasi over middle Indo-Gangetic Plain: variation in particulate types and meteorological
770   influences, Environ. Monit. Assess., 189(4), https://doi.org/10.1007/s10661-017-5859-9,
771   2017.

772 Neely, R. R., Yu, P., Rosenlof, K. H., Toon, O. B., Daniel, J. S., Solomon, S., and Miller, H. L.:
773   The contribution of anthropogenic SO2 emissions to the Asian tropopause aerosol layer, J.
774   Geophys. Res., 119(3), 1571–1579. https://doi.org/10.1002/2013JD020578, 2014.

775 Park, M., Randel, W. J., Gettelman, A., Massie, S. T., and Jiang, J. H.: Transport above the Asian
776   summer monsoon anticyclone inferred from Aura Microwave Limb Sounder tracers, J.
777   Geophys. Res.-Atmos., 112(16), 1–13, https://doi.org/10.1029/2006JD008294, 2007.

778 Pawar, G.V., Devara, P.C.S., and Aher, G.R.: Identification of aerosol types over an urban site
779   based on air-mass trajectory classification, Atmos. Res., 164-165, 142-155.
780   https://doi.org/10.106/j.atmosres.2015.04.022, 2015.

781 Randel, W. J., and Park, M.: Deep convective influence on the Asian summer monsoon anticyclone
782   and associated tracer variability observed with Atmospheric Infrared Sounder (AIRS), J.
783   Geophys. Res.-Atmos., 111(12), 1–13, https://doi.org/10.1029/2005JD006490, 2006.

784 Ratnam, M. V., Raj, S. T. A., Madhavan, B. L., Vernier, J. P., Kiran, V. R., Jain, C. D., Basha, G.,
785   Nagendra, N., Kumar, B. S., Pandit, A. K., Murthy, B. V. K., & Jayaraman, A.: Vertically
786   resolved black carbon measurements and associated heating rates obtained using in situ
787   balloon platform, Atmos. Environ., 232, https://doi.org/10.1016/j.atmosenv.2020.117541,
788   2020.

789 Ratnam, M.V, Sunilkumar, S. V., Parameswaran, K., Krishna Murthy, B. V., Ramkumar, G.,
790   Rajeev, K., Basha, G., Ravindra Babu, S., Muhsin, M., Kumar Mishra, M., Hemanth Kumar,
791   A., Akhil Raj, S. T., and Pramitha, M.: Tropical tropopause dynamics (TTD) campaigns over
792   Indian region: An overview, J. Atmos. Sol.-Terr. Phys., 121(PB), 229–239,
793   https://doi.org/10.1016/j.jastp.2014.05.007, 2014.

794 Ricchiazzi, P., Yang, S., Gautier, C., and Sowle, D.: SBDART: A research and teaching software
795   tool for plane-parallel radiative transfer in the Earth's atmosphere, *Bull. Am. Meteorol. Soc.*,
796   79, 2101–2114, 1998.

Santhosh, V. N., Madhavan, B. L., and Venkat Ratnam, M.: Quantifying shortwave radiative forcing and heating rates of UTLS aerosols in the Asian summer monsoon anticyclone region, *J. Quant. Spectrosc. Ra.*, 339, 109430, https://doi.org/10.1016/j.jqsrt.2025.109430, 2025.

Santhosh, V. N., Madhavan, B. L., Ratnam, M. V., Naik, D. N., and Sellitto, P.: Assessing biases in atmospheric parameters for radiative effects estimation in tropical regions, J. Quant. Spectrosc. Radiat. Transf., 314, 108858, https://doi.org/10.1016/j.jqsrt.2023.108858, 2024a.

Santhosh, V. N., Madhavan, B. L., Ratnam, M. V., and Naik, D. N.: Influence of columnar versus vertical distribution of aerosol properties on the modulation of shortwave radiative effects, J. Quant. Spectrosc. Radiat. Transf., 329, 109179, https://doi.org/10.1016/j.jqsrt.2024.109179, 2024b.

Sinha, P. R., Dumka, U. C., Manchanda, R. K., Kaskaoutis, D. G., Sreenivasan, S., Krishna Moorthy, K., and Suresh Babu, S.: Contrasting aerosol characteristics and radiative forcing over Hyderabad, India due to seasonal mesoscale and synoptic-scale processes, Q. J. R. Meteorol. Soc., 139(671), 434–450. https://doi.org/10.1002/qj.1963, 2013.

Solomon, S., Daniel, J. S., Neely, R. R., Vernier, J. P., Dutton, E. G., and Thomason, L. W.: The persistently variable "background" stratospheric aerosol layer and global climate change, Science, 333(6044), 866–870, https://doi.org/10.1126/science.1206027, 2011.

Stamnes, K., Tsay, S.-C., Wiscombe, W., and Jayaweera, K.: Numerically stable algorithm for discrete-ordinate-method radiative transfer in multiple scattering and emitting layered media, App. Opt., 27(12), 2502, https://doi.org/10.1364/ao.27.002502, 1988.

Stein, A. F., Draxler, R. R., Rolph, G. D., Stunder, B. J. B., Cohen, M. D., and Ngan, F.: NOAA's hysplit atmospheric transport and dispersion modeling system, Bull. Amer. Meteor. Soc., 96(12), 2059–2077, https://doi.org/10.1175/BAMS-D-14-00110.1, 2015.

Thomason, L. W., and Vernier, J. P.: Improved SAGE II cloud/aerosol categorization and observations of the Asian tropopause aerosol layer: 1989-2005, Atmos. Chem. Phys., 13(9), 4605–4616, https://doi.org/10.5194/acp-13-4605-2013, 2013.

Tiwari, S., and Singh, A. K.: Variability of Aerosol parameters derived from ground and satellite measurements over Varanasi located in the Indo-Gangetic Basin, Aerosol Air Qual. Res., 13(2), 627–638. https://doi.org/10.4209/aaqr.2012.06.0162, 2013.

Vernier, H., Rastogi, N., Liu, H., Pandit, A. K., Bedka, K., Patel, A., Ratnam, M. V., Kumar, B. S., Zhang, B., Gadhavi, H., Wienhold, F., Berthet, G., and Vernier, J. P.: Exploring the inorganic composition of the Asian Tropopause Aerosol Layer using medium-duration balloon flights, Atmos. Chem. Phys., 22(18), 12675–12694. https://doi.org/10.5194/acp-22-12675-2022, 2022.

Vernier, J. P., Fairlie, T. D., et al.: BATAL: The balloon measurement campaigns of the Asian

832 tropopause aerosol layer, Bull. Am. Meteor. Soc., 99(5), 955–973,
833   https://doi.org/10.1175/BAMS-D-17-0014.1, 2018.

834 Vernier, J. P., Thomason, L. W., and Kar, J.: CALIPSO detection of an Asian tropopause aerosol
835   layer, Geophys. Res. Lett., 38(7), 1–6, https://doi.org/10.1029/2010GL046614, 2011.

836 Vernier, J.-P., T. D. Fairlie, M. Natarajan, F. G. Wienhold, J. Bian, B. G. Martinsson, S.
837   Crumeyrolle, L. W. Thomason, and K. M. Bedka: Increase in upper tropospheric and lower
838   stratospheric aerosol levels and its potential connection with Asian pollution, J. Geophys.
839   Res.-Atmos., 120, 1608–1619, https://doi.org/10.1002/2014JD022372, 2015.

840 Vogel, B., Volk, C. M., Wintel, J., Lauther, V., Clemens, J., Grooß, J.-U., Günther, G., Hoffmann,
841   L., Laube, J. C., Müller, R., Ploeger, F., & Stroh, F.: Evaluation of vertical transport in ERA5
842   and ERA-Interim reanalysis using high-altitude aircraft measurements in the Asian summer
843   monsoon 2017. *Atmospheric Chemistry and Physics*, *24*(1), 317–343.
844   https://doi.org/10.5194/acp-24-317-2024, 2024.

845 Von Hobe, M., Ploeger, F., Konopka, P., Kloss, C., Ulanowski, A., Yushkov, V., Ravegnani, F.,
846   Volk, C. M., Pan, L. L., Honomichl, S. B., Tilmes, S., Kinnison, D. E., Garcia, R. R., &
847   Wright, J. S.: Upward transport into and within the Asian monsoon anticyclone as inferred
848   from StratoClim trace gas observations. *Atmospheric Chemistry and Physics*, *21*(2), 1267–
849   1285. https://doi.org/10.5194/acp-21-1267-2021, 2021.

850 Xu, H., Guo, J., Tong, B., Zhang, J., Chen, T., Guo, X., Zhang, J., and Chen, W.: Characterizing
851   the near-global cloud vertical structures over land using high-resolution radiosonde
852   measurements, Atmos. Chem. Phys., 23(23), 15011–15038. https://doi.org/10.5194/acp-23-
853   15011-2023, 2023.

854 Yu, P., Lian, S., Zhu, Y., Toon, O. B., Höpfner, M., and Borrmann, S.: Abundant Nitrate and Nitric
855   Acid Aerosol in the Upper Troposphere and Lower Stratosphere, Geophys. Res. Lett., 49(18),
856   https://doi.org/10.1029/2022GL100258, 2022.

857 Yu, P., Rosenlof, K. H., Liu, S., Telg, H., Thornberry, T. D., Rollins, A. W., Portmann, R. W.,
858   Bai, Z., Ray, E. A., Duan, Y., Pan, L. L., Toon, O. B., Bian, J., & Gao, R.-S.: Efficient
859   transport of tropospheric aerosol into the stratosphere via the Asian summer monsoon
860   anticyclone. *Proceedings of the National Academy of Sciences*, *114*(27), 6972–6977.
861   https://doi.org/10.1073/pnas.1701170114, 2017.

862 Yu, P., Toon, O. B., Neely, R. R., Martinsson, B. G., and Brenninkmeijer, C. A. M.: Composition
863   and physical properties of the Asian Tropopause Aerosol Layer and the North American
864   Tropospheric Aerosol Layer, Geophys. Res. Lett., 42(7), 2540–2546.
865   https://doi.org/10.1002/2015GL063181, 2015.

866 Zhang, H., Shen, Z., Wei, X., Zhang, M., and Li, Z.: Comparison of optical properties of nitrate
867   and sulfate aerosol and the direct radiative forcing due to nitrate in China, Atmos. Res., 113,

868   113–125, https://doi.org/10.1016/j.atmosres.2012.04.020, 2012.

869 Zhu, Y., Yu, P., Wang, X., Bardeen, C., Borrmann, S., Höpfner, M., Mahnke, C., Weigel, R.,
870   Krämer, M., Deshler, T., Bian, J., Bai, Z., Vernier, H., Portmann, R. W., Rosenlof, K. H.,
871   Kloss, C., Pan, L. L., Smith, W., Honomichl, S., … Toon, O. B.: Evaluating the Importance
872   of Nitrate-Containing Aerosols for the Asian Tropopause Aerosol Layer. *Journal of*
873   *Geophysical   Research: Atmospheres*,   *129*(19),   e2024JD041283.
874   https://doi.org/10.1029/2024JD041283, 2024.